Single-source rapid-repeat time-lapse elastic FWI based on the DAS-VSP data

Xiaohui Cai, Kris Innanen, Don Lawton

ABSTRACT

Last year, to track the transient changing levels of CO_2, we employed elastic full waveform inversion (EFWI) to identify anomalies in single-source rapid-repeat time-lapse VSP data. The time-lapse EFWI inversion outcomes, relying on differences in data norms, have demonstrated their ability to identify and assess changes in time-lapse data caused by the injection of CO_2. However, the data norm difference response only in the geophone data instead of the distributed acoustic sensing (DAS) data. In theory, the injection of CO_2 into the formation is expected to change the elastic parameters, resulting in noticeable changes in the difference between the shot gathers before and after the injection. This change typically manifests as distinct upgoing wavefield data. Therefore, we develop an inversion strategy that relies on the difference of upgoing DAS data This strategy aims to determine whether it can effectively detect transient changes based on DAS data during the injection of CO_2.

INTRODUCTION

CO_2 monitoring ensures the effectiveness of geological storage after CO_2 is injected into the ground and prevents environmental hazards caused by possible CO_2 leakage. Time-lapse vertical seismic profile (VSP) surveys are likely to be a key technology for monitoring CO_2 injection and verifying containment and storage. Practical and low-cost measurement, monitoring, and validation are significant gaps in technology for large-scale implementation of carbon storage. In 2022, a time-lapse rapid-repeated VSP survey called Tiny Bubbles was carried out at Carbon Management Canada's (CMC) Newell County Facility, using geophone and collocated distributed acoustic sensing (DAS) fiber within an observation well situated at the field site. This facility serves as a dedicated platform for the development and validation of technologies aimed at measuring, monitoring, and verifying CO_2 storage, as outlined in studies by (Lawton et al., 2019) and (Macquet et al., 2019). Last year, we proposed a time-lapse elastic full waveform inversion (ERTM) workflow based on rapid-repeat data norm differences to detect the dynamic change of elastic parameter during the CO_2 injection. This year, we are exploring an alternative method that concentrates on DAS data to examine whether the Tiny bubble DAS data can detect the changes occurring during the injection of CO_2.

The utilization of DAS data has burgeoned in recent years, marking a pivotal advancement in academic research and scientific inquiry. This technology has transcended traditional sensor capabilities by repurposing existing fiber optic infrastructure into an extensive and versatile sensing network. Its application spans many disciplines, offering a wealth of high-fidelity data that facilitates unparalleled insights into dynamic phenomena across various domains. As an innovative tool in geophysics, civil engineering, environmental monitoring, and beyond, DAS data stands at the forefront of cutting-edge research, propelling the boundaries of knowledge and understanding within academia. This introduction aims

to elucidate DAS data's profound impact and multifaceted applications in contemporary scholarly endeavors.

METHOD

Our FWI workflow includes inversion for the DAS data, as discussed in Eaid et al. (2020). We use a two-order frequency-domain regular-grid finite-differences method to solve the isotropic displacement elastic wave equation Pratt (1990) and apply the perfectly matching layer to suppress the boundary reflections Berenger (1994). For establishing our inversion procedure, we obtain the 1D starting model by smoothing and extrapolating the available well log data, where the part of data was interpreted by the soft-sand model and Gassmann's equations Hu and Innanen (2019) to provide P-wave sonic, S-wave sonic, and density logs (0 - 223 m) and the other is acquired by well logs (224 m - 350 m).

We use codes originally developed for multi-parameter elastic FWI by (Keating et al., 2021). The optimization process utilizes the Limited-memory Broyden-Fletcher-Goldfarb-Shanno (L-BFGS) algorithm. The selection of suitable parameterization holds paramount importance in FWI Pan et al. (2018), and the parameterization with V_p, V_s, and ρ proves to be a suitable choice for conducting FWI on VSP data, primarily due to the prevalence of transmitted arrivals which exhibit heightened energy characteristics Roberts et al. (2008). Based on the strong correlation between V_p and V_s, V_p and ρ in the study field Eaid et al. (2023), we use P-velocity (V_p)-parameterized to helps reduce cross-talk by only allowing updates in one parameter.

To mitigate the nonlinearity of the inverse problem, a multiscale strategy Bunks et al. (1995) is applied. We examine five frequency bands, with each band comprising twelve evenly distributed frequencies ranging from minimum to maximum frequency for 10 to 75 Hz. The frequency step takes approximately 20 iterations for baseline data and 50 iterations for monitor data. No regularization is used during the inversion, but a Gaussian layered constraint with 8 m is applied after the inversion.

Effective Source Estimation

Various approaches exist for selecting an appropriate source wavelet for the inversion process. We use an effective source approach Keating et al. (2021) to take into account incomplete near-surface model information, source characteristics, and wavefield physics. In the effective source estimation, we assume a line source at a depth that generates the wavefield that would be obtained by propagation through the near-surface. We invert for both model parameters and the unknown source.

Time-Lapse Strategy

We apply the double-difference time-lapse approach. To start, the baseline inversion is based on the initial model from the well-log data and baseline field data. Next, the monitor inversions use the initial model obtained from the baseline inverted model. Then, we generate modeled data using the baseline inverted model and add the difference between the monitor and baseline field data to this modeled data, treating it as the observed monitor

field data. Finally, the monitor inversion is based on the updated monitor initial model and observed field data.

FIELD DATA INVERSION

Background

In January 2022, Carbon Management Canada (CMC) Newell County Facility conducted a rapid-repeat time-lapse VSP seismic trial, named "Tiny Bubble," in the vicinity of Brooks, Alberta. This experiment involved injecting CO_2 into a shallow Upper Cretaceous Basal Belly River sandstone unit at a depth of 300 meters (Isaac and Lawton, 2016). The goal was to perform a repeat seismic shot with ray-paths intersecting the anticipated fluid to detect any transient alterations. The experiment's layout is outlined in Figure 1. Upon introduction, the CO_2 entered the Basal Belly River Sandstone (BBRS) formation, generating pressure and fluid plumes within the 290-305 meter depth range. The DAS fiber extended from 0 to 337 meters, muting data above 80 meters for the low signal-to-noise ratio. The source was located 215 meters from the observation well, and the injection well was situated between the source and the observation well, offset by 20 meters from the observation well. Moreover, the estimated pressure plume was situated at 267 meters near the injection well. We concentrated on transient changes within the medium by rapid-repeat seismic shots.

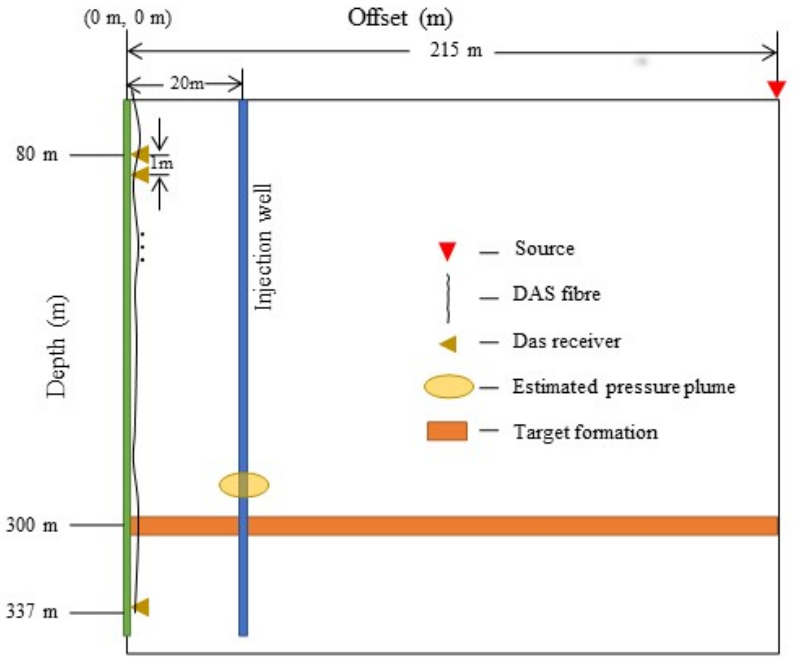

FIG. 1. Geometry of Tinybubble seismic source, injection and observation wells.

Dataset overview

The depth of DAS data is unknown, and we apply the depth registration method to get the DAS data locations, where the details can be seen in (Cai et al., 2022). Figure 2 shows

the pressure change at 267 m from Jan 17 to Jan 22, 2022. There are 64 clusters during the time, and we select the 10 clusters data (clusters 1, 3, 5, 13, 22, 31, 39, 47, 56, 64) to display the field data and their analysis conveniently. The selected 10 clusters have their features: (1) cluster 1 is the baseline. (2) cluster 3 occurred at similar times with cluster 1; (3) cluster 5 occurred around the beginning of the first CO_2 injection; (4) cluster 13 occurred during the first CO_2 injection; (5) cluster 22 occurred at the end of the first CO_2 injection; (6) cluster 31 occurred between the twice CO_2 injection; (7) cluster 39 occurred around the beginning of the second CO_2 injection; (8) cluster 47 is during the second CO_2 injection; (9) cluster 56 occurred at the end of the second CO_2 injection; (10) cluster 64 occurred at the end of the experiment.

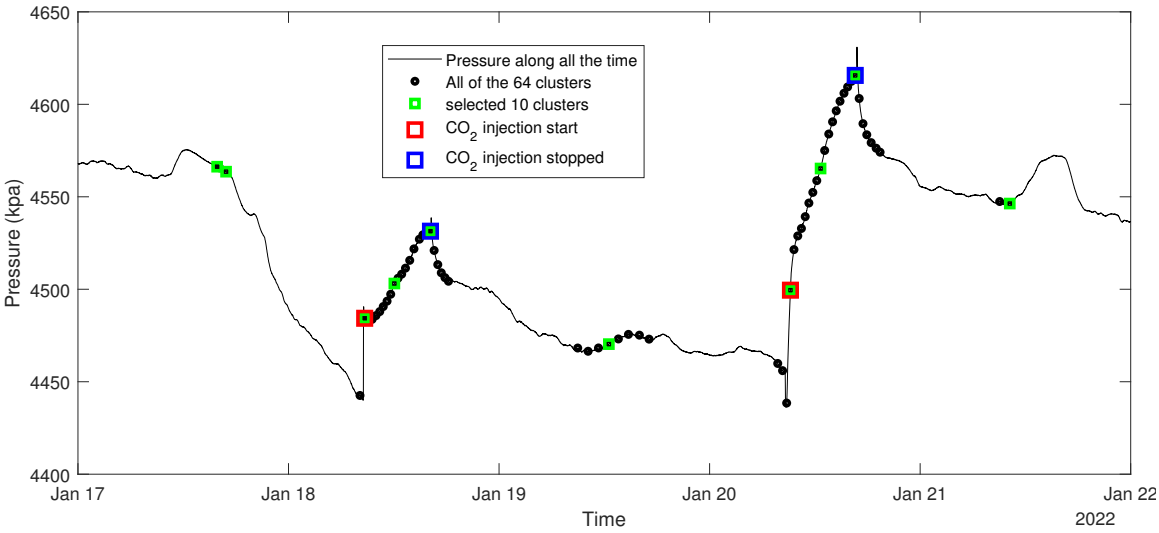

FIG. 2. Pressure change at 267 m (black curve) along the time from Jan 17 to Jan 22, 2022. Black circles are the times at which all 64 monitoring shot clusters occurred. Red squares and blue squares indicate the start and end of CO_2 injection, respectively.

To analyze the field data, we compare the monitor data with the baseline data for the selected clusters. Figure 3 displays the baseline data (a) and illustrates the differences between the baseline data and the selected 9 monitor data points (b-j). From the observed differences, it's evident that with increased injection time, the variations between each monitoring and baseline survey line alter noticeably. Notably, these differences predominantly consist of downgoing wavefields without any conspicuous presence of upgoing wavefields. Referring to the schematic diagram in Figure 4 and considering the current geometry, focusing the inversion on the downgoing waves between the baseline survey line and the monitoring line yields an illumination of up to approximately 20 m around the well. However, conducting inversion based on the upgoing waves' differences extends the illumination of the target layer to nearly 90 m. Therefore, we perform the upgoing and downgoing wavefield separation by FK filtering for all monitor data in Figure 3 (b)-(j). Figure 5 illustrates the separated downgoing wavefields, while Figure 6 displays the separated upgoing wavefields. The updated monitoring line data is generated by combining the baseline data with the separated upgoing wavefields.

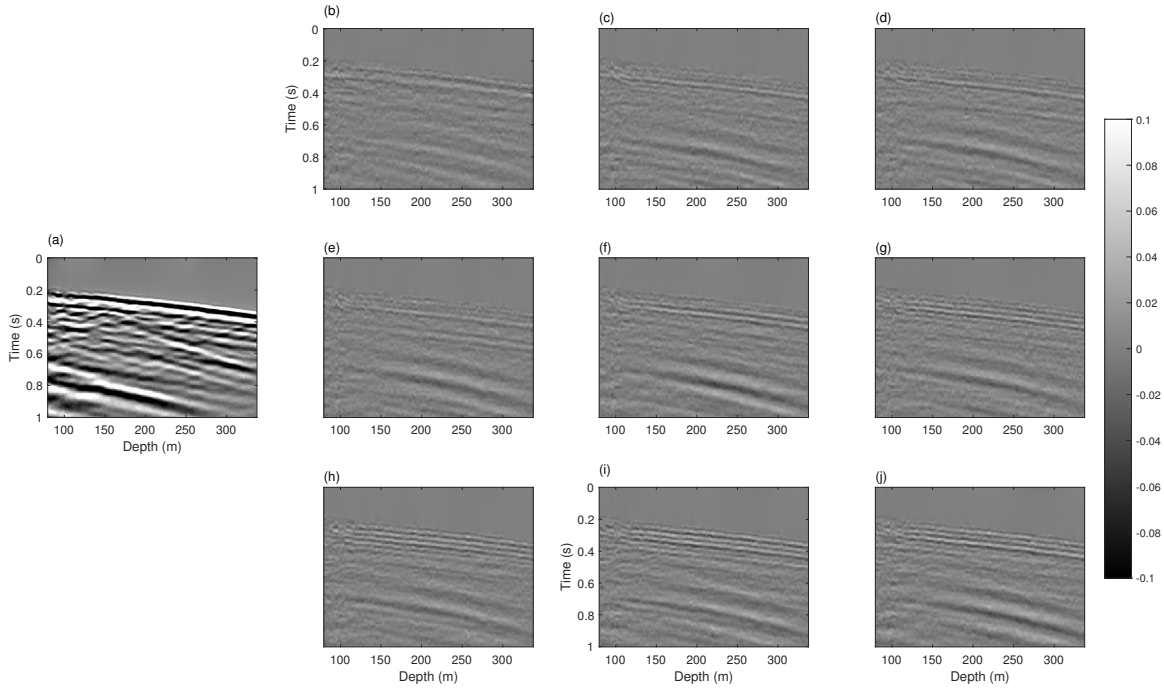

FIG. 3. (a) The processed baseline cluster 1 data. (b)-(j) represents the data difference between clusters 3, 5, 13, 22, 31, 39, 47, 56, and 64 compared to the cluster 1 baseline.

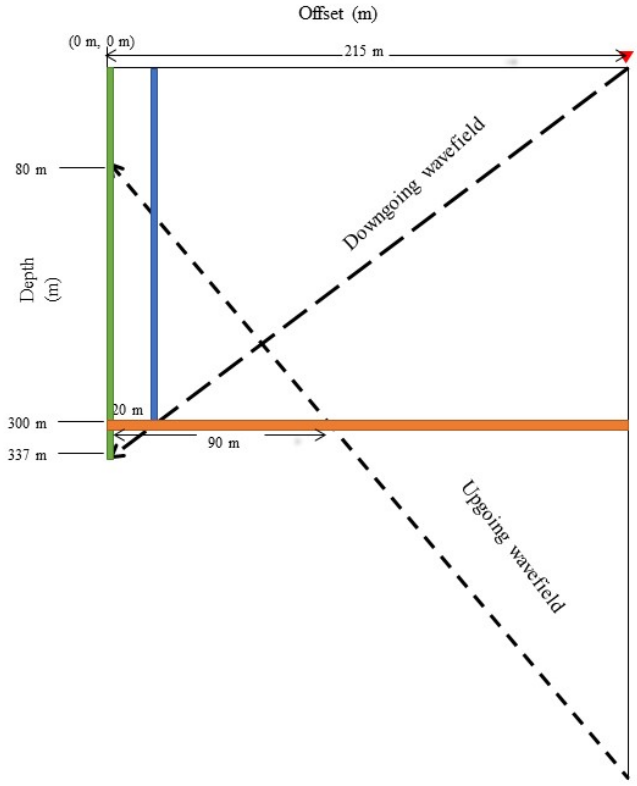

FIG. 4. (a) The schematic diagram for the upgoing and downgoing wavefields based on the Tiny bubble geometry.

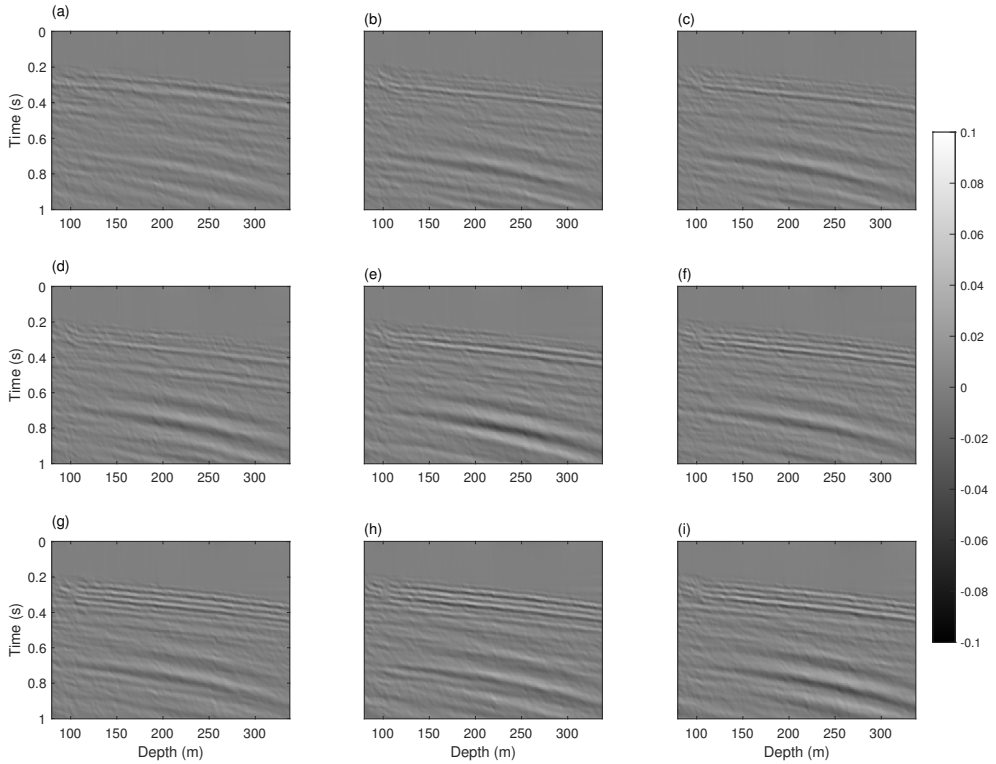

FIG. 5. (a)-(i) represents the separated downgoing wavefields difference between clusters 3, 5, 13, 22, 31, 39, 47, 56, and 64 compared to the cluster 1 baseline data.

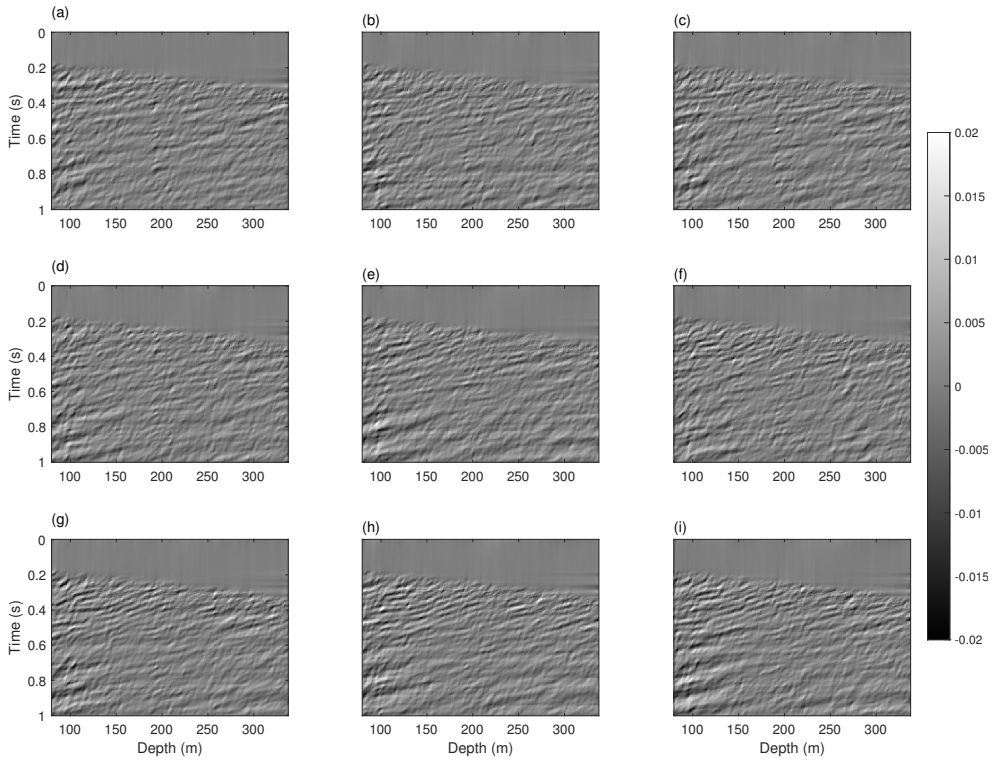

FIG. 6. (a)-(i) represents the separated upgoing wavefields difference between clusters 3, 5, 13, 22, 31, 39, 47, 56, and 64 compared to the cluster 1 baseline data.

Inversion

We use P-wave velocity parameterization frequency-domain FWI and effective source estimation schemes to implement the elastic properties inversion. The model size is 240 m in the x-direction and 350 m in the z-direction, and the space interval is 5 m. Figure 7 shows the initial and inverted models of V_{p}, V_{s}, and ρ for baseline data, and Figure 9 shows the comparison of the initial and inverted velocities models with the well logs data. In addition, Figure 8 indicates snapshots of the inverted time-lapse V_p model, which include the injection well (red line), the injection depth (rose red dash line), injection hours, and the amount of CO_2 injection. At injection locations (around injection location 300 m), clusters 13, 22, 31, 47, 56, and 64 exhibit velocity anomalies. However, the energy level of the valid anomaly signals is comparable to the surrounding noise, posing challenges in distinguishing between valid anomalies and noise.

Let's consider cluster 56 as an example from the monitor line. For quality control purposes, we conduct a comparison between the inverted offset VSP gathers and the field data in both the frequency domain, as depicted in Figures 10 and 11, and the time domain, represented in Figure 12. Figures 10 and 11 present the frequency-domain field data (top), the inverted effective source data (middle), and the modeled data based on the inverted baseline and monitor models, respectively (bottom). Figure 12 displays the baseline and modeled field data, and their differences in the top row. Additionally, it exhibits the difference between the modeled monitor and baseline data, the modeled monitor data, and the difference between the monitor field data and modeled data in the bottom row. Upon comparison, we observe a satisfactory agreement between the field and modeled data for both the baseline and monitor lines. Moreover, a notable agreement exists in the differences between the baseline and monitor lines, visible in comparison of Figure 12 and Figure 6.

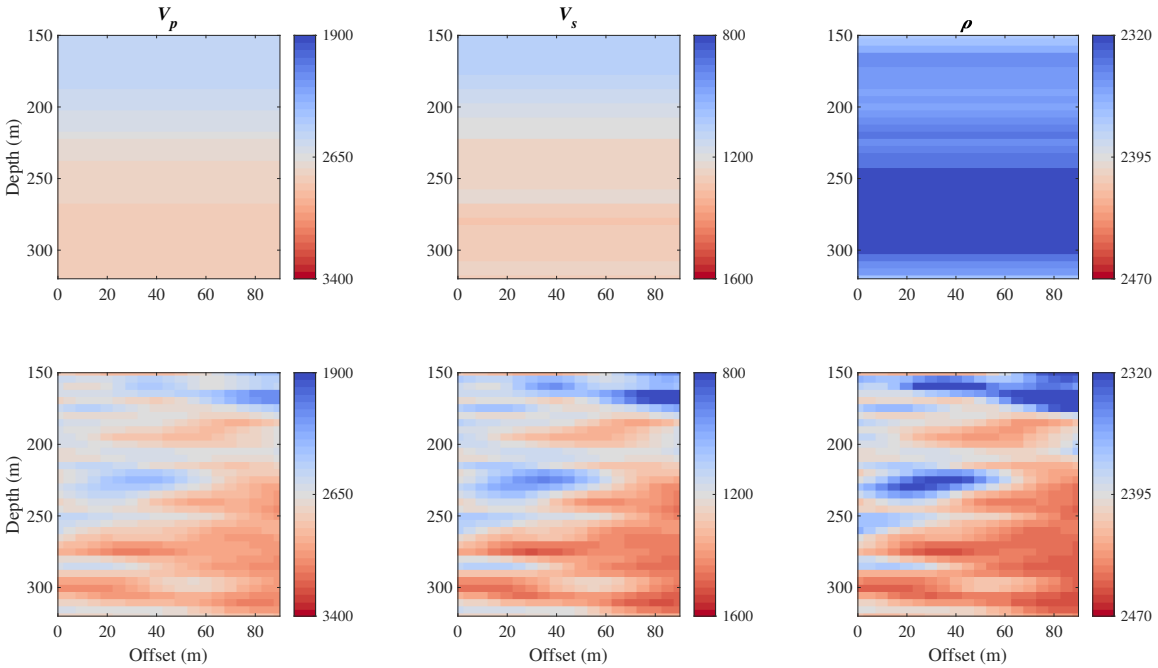

FIG. 7. The inverted models of V_{p}, V_{s}, and ρ for cluster 1 (baseline data).

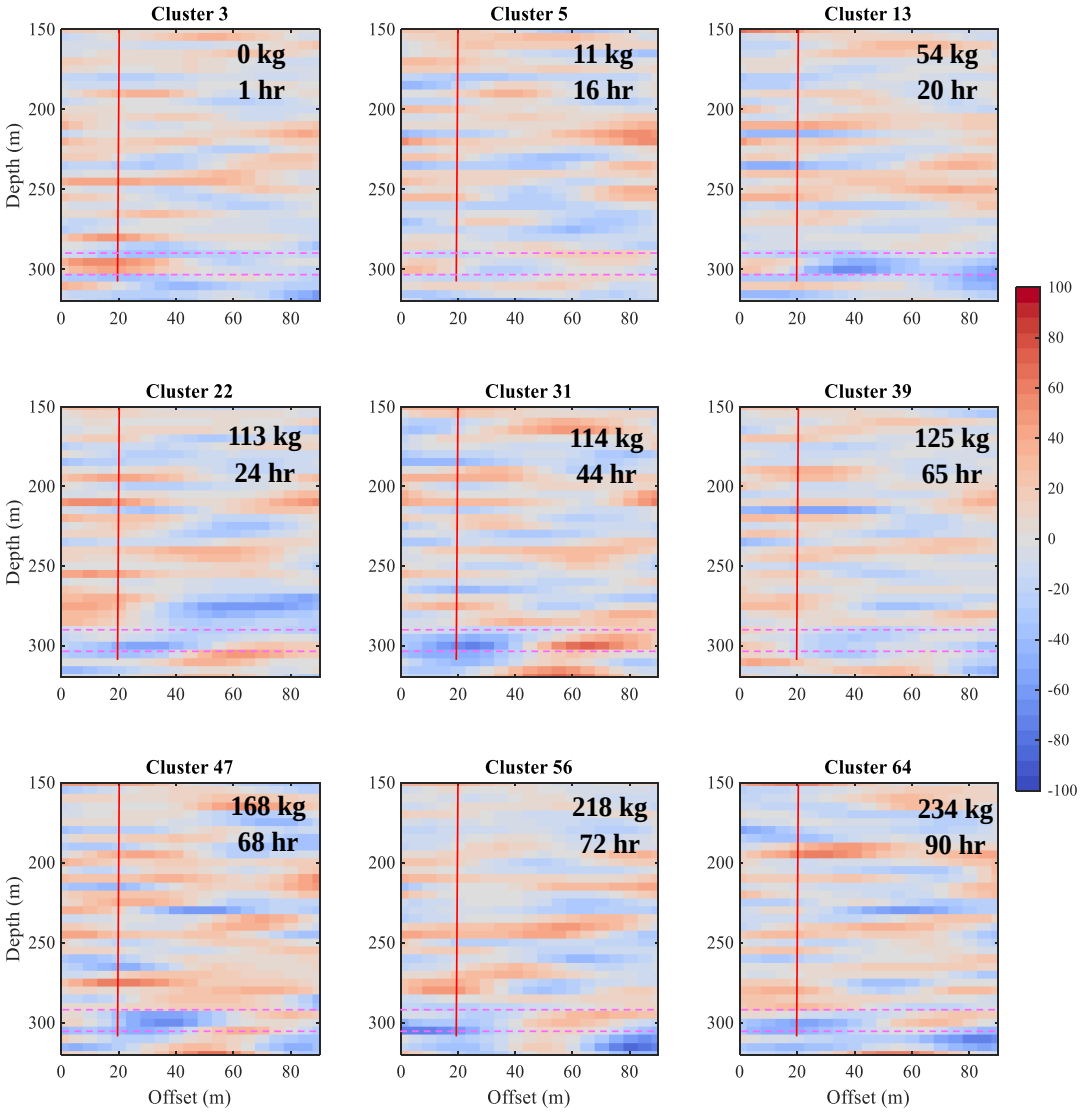

FIG. 8. The inverted V_{P} models difference between the 9 monitor data and baseline.

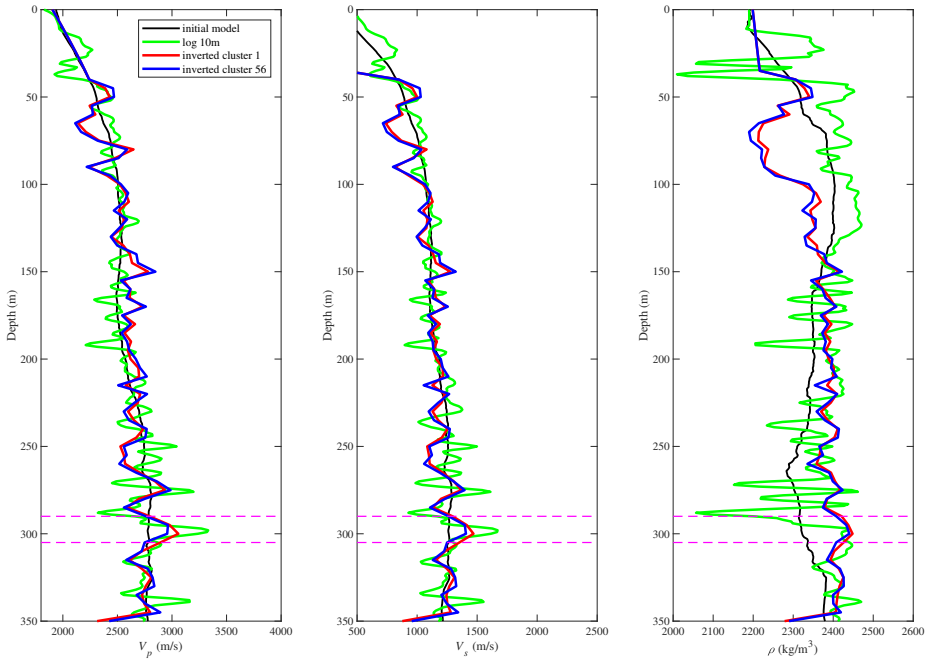

FIG. 9. The comparison of the initial and inverted velocities models with the well logs data.

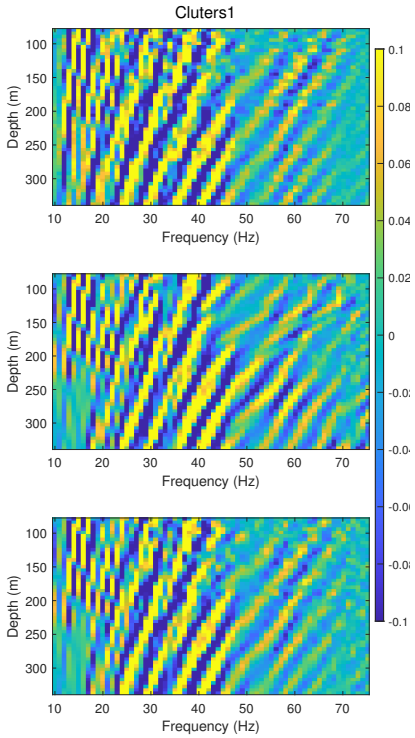

FIG. 10. The frequency-domain field data (top), the inverted effective source data (middle), and the modeled data based on the inverted baseline model.

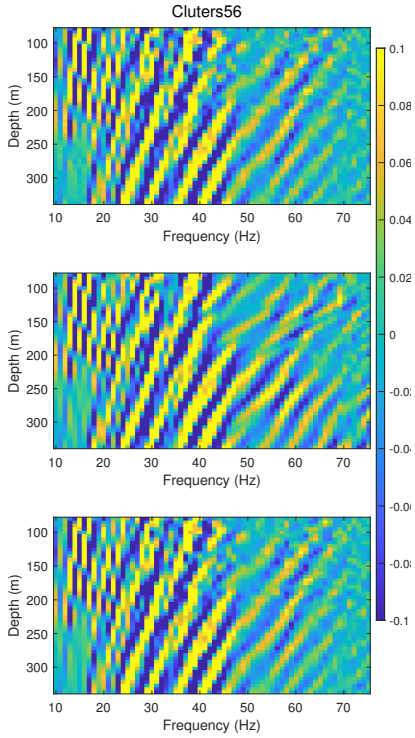

FIG. 11. The frequency-domain field data (top), the inverted effective source data (middle), and the modeled data based on the inverted monitor model.

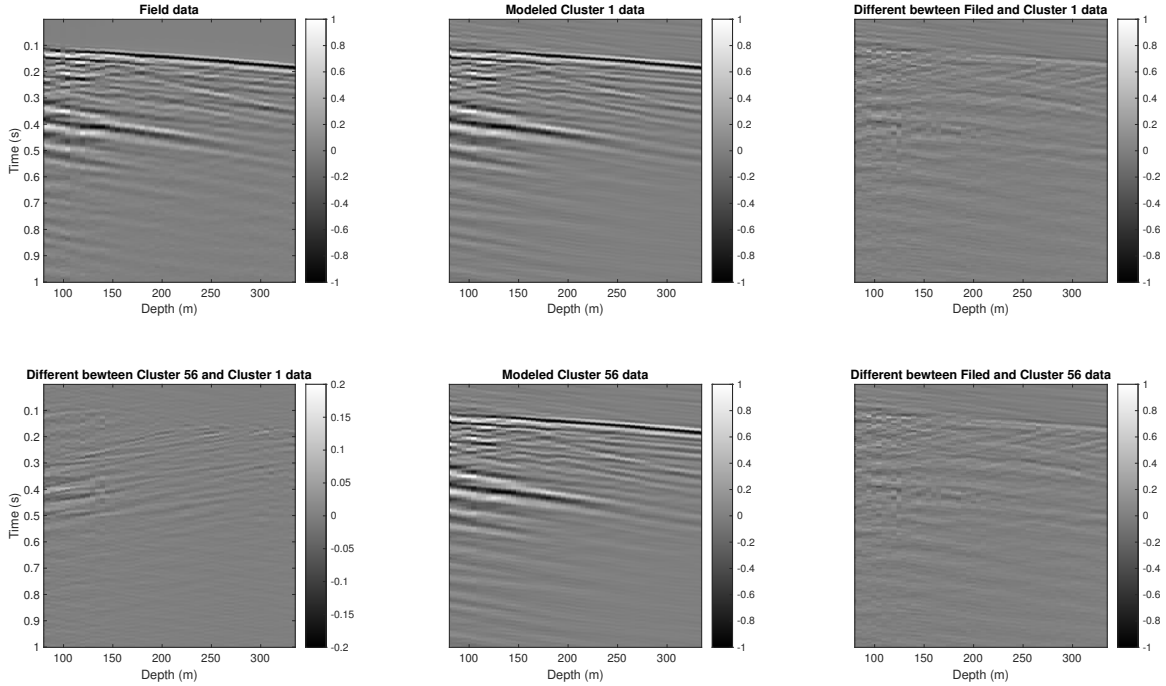

FIG. 12. The comparison between the inverted offset VSP gathers and the field data in the time domain.

DISCUSSION

The difference in the upgoing wavefield between the baseline and monitoring lines illustrates alterations in energy with the injection of carbon dioxide in Figure 6. These alterations in energy are somewhat subtle. In addition, the difference is relatively weaker than the downgoing wavefield or background noise. This distinction poses a challenge in differentiating valid anomalies from noise in the final time-lapse snapshots. If it were possible to remove background noise and extract high-precision upgoing wave energy entirely, it might lead to time-lapse snapshots with a higher signal-to-noise ratio. This improvement could potentially enhance the clarity and accuracy of the final inversion results.

CONCLUSIONS

Based on the characteristics of rapid-repeated time-lapse data with only one location source, a time-lapse frequency inversion method was developed based on the upgoing data difference. The outcomes from conducting 2D EFWI on offset DAS-VSP data indicate the capability of this technology to yield high-resolution models depicting the subsurface's physical properties. However, the challenge arises with the single-source rapid-repeated time-lapse DAS-VSP EFWI detecting anomalies in parameters such as V_p, V_s, and ρ. This difficulty might be due to its relatively lower sensitivity compared to geophone data, making it harder to identify the location and trends of anomalies compared with last year's combined geophone and DAS data time-lapse inversion results.

ACKNOWLEDGMENTS

The sponsors of CREWES are gratefully thanked for continued support. This work was funded by CREWES industrial sponsors, NSERC (Natural Science and Engineering Research Council of Canada) through the grant CRDPJ 543578-19. This work was done in collaboration with the Carbon Management Canada.

REFERENCES

Berenger, J. P., 1994, A perfectly matched layer for the absorption of electromagnetic waves: Journal of computational physics, **114**, No. 2, 185–200.

Bunks, G., Saleck, F. M., Zaleski, S., and Chavent, G., 1995, Multiscale seismic waveform inversion: Geophysics, **60**, No. 5, 1457–1473.

Cai, X., Innanen, K., Zhang, T., Eaid, M., Keating, S., Hall, K., and Lawton, D., 2022, Analysis of the fwi workflow for geophone and DAS data from the 2018 CaMI VSP survey: CREWES Research Reports.

Eaid, M. V., Keating, S. D., and Innanen, K. A., 2020, Multiparameter seismic elastic full-waveform inversion with combined geophone and shaped fiber-optic cable data: Geophysics, **85**, No. 6, R537–R552.

Eaid, M. V., Keating, S. D., Innanen, K. A., Macquet, M., and Lawton, D., 2023, Field assessment of elastic full waveform inversion of combined accelerometer and distributed acoustic sensing data in a vertical seismic profile configuration: Geophysics, **88**, No. 6, 1–68.

Hu, Q., and Innanen, K., 2019, Rock physics analysis for the well-log data at CaMI FRS: CREWES Research Reports.

Isaac, J. H., and Lawton, D. C., 2016, Brooks revisited: CREWES Research Reports.

Keating, S., Eaid, M., and Innanen, K., 2021, Effective sources: removing the near surface from the vsp fwi problem: CREWES Report.

Lawton, D. C., Dongas, J., Osadetz, K., Saeedfar, A., and Macquet, M., 2019, Development and analysis of a geostatic model for shallow CO_2 injection at the field research station, southern alberta, canada: Geophysics and Geosequestration. Cambridge University Press, Cambridge, **280**, 296.

Macquet, M., Lawton, D. C., Saeedfar, A., and Osadetz, K. G., 2019, A feasibility study for detection thresholds of co2 at shallow depths at the cami field research station, newell county, alberta, canada: Petroleum Geoscience, **25**, No. 4, 509–518.

Pan, W. Y., Geng, Y., and Innanen, K. A., 2018, Interparameter trade-off quantification and reduction in isotropic-elastic full-waveform inversion: synthetic experiments and hussar land data set application: Geophysical Journal International, **213**, No. 2, 1305–1333.

Pratt, R. G., 1990, Frequency-domain elastic wave modeling by finite differences: A tool for crosshole seismic imaging: Geophysics, **55**, No. 5, 626–632.

Roberts, M. A., Singh, S., and Hornby, B. E., 2008, Investigation into the use of 2d elastic waveform inversion from look-ahead walk-away vsp surveys: Geophysical prospecting, **56**, No. 6, 883–895.